Electrochemical Conversion of Alcohols into Acidic Commodities on Nickel Sulfide Nanoparticles

Junshan Li,[a] Xi Tian,[b] Xiang Wang,[c] Ting Zhang,[d] Maria Chiara Spadaro,[d] Jordi Arbiol,[d,e] Luming Li,[b*] Yong Zuo,[c*] Andreu Cabot[c,e*]

a Institute for Advanced Study, Chengdu University, 610106, Chengdu, China

b College of Food and Biological Engineering, Chengdu University, Chengdu 610106, China

c Catalonia Institute for Energy Research - IREC, Sant Adrià de Besòs, Barcelona, 08930, Catalonia, Spain.

d Catalan Institute of Nanoscience and Nanotechnology (ICN2), CSIC and BIST, Campus UAB, Bellaterra, 08193 Barcelona, Catalonia, Spain.

e ICREA, Pg. Lluís Companys 23, 08010 Barcelona, Catalonia, Spain.

Abstract: The electrocatalytic oxidation of alcohols is a potentially cost-effective strategy for the synthesis of valuable chemicals at the anode while simultaneously generating hydrogen at the cathode. For this approach to become commercially viable, high activity, low-cost, and stable catalysts need to be developed. Herein, we demonstrate an electrocatalyst based on earth-abundant nickel and sulfur elements. Experimental investigations reveal the produced NiS displays excellent electrocatalytic performance associated with a higher electrochemical surface area (ECSA) and the presence of sulfate ions on the formed NiOOH surface in basic media. The current densities reached for the oxidation of ethanol and methanol at 1.6 V vs. RHE are up to 175.5 and 145.1 mA cm^{-2}, respectively. At these high current densities, the Faradaic efficiency of methanol to formate conversion is 98%, and that of ethanol to acetate is 81%. Density functional theory calculations demonstrate the presence of the generated sulfate groups to modify the electronic properties of the NiOOH surface, improving electroconductivity and electron transfer. Besides, calculations are used to determine the reaction energy barriers, revealing the dehydrogenation of ethoxy groups to be more favourable than that of methoxy on the catalyst surface, which explains the highest current densities obtained for ethanol oxidation.

Keywords: nickel, nickel sulfide; methanol oxidation reaction; ethanol oxidation reaction; electrochemical reforming; hydrogen, electrocatalysis.

Introduction

With the increasing concern about global warming and environmental pollution, the search for clean energy carriers as an alternative to fossil fuels has intensified.[1] In this context, hydrogen is considered an ideal energy carrier with zero carbon emissions.[2] However, hydrogen production still relies on the use of fossil fuels. Thus alternative hydrogen production strategies and hydrogen sources are required.[3]

Thermodynamics imposes a minimum of 1.23 V to drive the electrocatalytic water splitting, but practical water electrolysis requires no less than 1.8 V due to the sluggish kinetics of the oxygen evolution reaction (OER) at the anode. Actually, the largest part of the additional energy consumed in the process is related to the production of oxygen, which is generally a discarded product owing to its low value.[4] To increase the process efficiency, more favourable anode reactions based on the oxidation of organic molecules, such as alcohols and amines, have been proposed to replace OER.[5–8] This strategy not only largely promotes the hydrogen evolution reaction (HER) at the cathode, but also generates a valuable side-product at the anode. Indeed, the selective oxidation of some of these organic molecules results in high purity commodity chemicals. This green chemical synthesis route at ambient temperature can be competitive with traditional industrial processes requiring high temperatures and pressures to produce some electrocatalylitically-accessible chemicals. This is the case of formate for instance, with an annual demand of 100 Mt.[9–11]

For the electrochemical process to become cost-effective, noble-metal-free and durable electrocatalysts need to be developed. Among other Earth-abundant elements, nickel-based catalysts have been reported to exhibit excellent electrocatalytic performances towards a plethora of electrocatalytic reactions, including the electro-oxidation of Cn alcohols (C1 = methanol, C2 = ethanol).[12–14]

Compared with monometallic Ni electrocatalysts, the use of Ni chalcogenides has been demonstrated to improve performance toward the OER[15–18], methanol oxidation reaction (MOR)[19–21] and ethanol oxidation reaction (EOR),[22–25] among others.[26–28] This improvement is generally ascribed to a bulk-driven modulation of the surface electronic structures of the Ni

catalyst, accelerating the metal regeneration in an alkaline medium. In addition, the presence of the ions produced from the chalcogen oxidation, e.g. sulfates, can change the local coordination environment of the active species regulating the adsorption of the reactants/intermediates/products.[29]

To maximize cost-effectiveness, catalysts need to be produced in the form of nanometric-size particles using cost-effective and scalable methods. In this direction, the Brutchey group has pioneered an "alkahest solvent" method for the high-throughput synthesis of chalcogenide nanoparticles (NPs). The alkahest solvent mixture is composed of ethanedithiol (Edt) and ethylenediamine (En) to dissolve a series of V_2VI_3 chalcogenides, such as As_2S_3, Sb_2S_3, Bi_2S_3, Bi_2Se_3, Bi_2Te_3 at room temperature, and then recover them in the form of nanostructured materials after annealing.[30] Such amine-thiol solution dissolves bulk chalcogens resulting in alkyl di-, tri- and tetrachalcogens, with –SR species binding to the metal ions, through an amine-catalyzed reaction.[30–32] In this amine-thiol system, the main difficulty is to prevent the formation of secondary phases, which generally requires proper control of the amine-thiol ratio and the reaction conditions.[33] Besides the metal precursor counter ions, eg, Cl^-, also affect the purity of recovered material, thus pure elemental precursors are generally chosen to avoid contamination.[33]

Herein, we detail the synthesis of nickel sulfur NPs using amine-thiol solutions and study their performance towards ethanol and methanol oxidation at high current density. To gain an understanding of the obtained results, we also conduct DFT calculations. We particularly analyze the effect of sulfate on the surface electronic structure and compare the mechanism of C1 and C2 alcohol oxidation on the same electrocatalysts, which has been very rarely reported.[13,34–36] The obtained results help to understand why ethanol can be more easily oxidized than methanol.

Experimental Section

Chemicals. All chemicals, including nickel powder (Ni, spherical, -400 mesh, 98 %, Alfa Aesar, nickel(II) acetylacetonate ($Ni(acac)_2 \cdot 2H_2O$, 95%, Sigma-Aldrich), sulfur powder (S, 99.98%, Sigma-Aldrich), ethylenediamine (En, 99.5%, Sigma-Aldrich), 1,2-ethanedithiol (Edt, 98%, Sigma-Aldrich), potassium hydroxide (KOH, 85%, Fisher), tri-n-octylphosphine (TOP, 97%, Strem), oleylamine (OAm, 80-90%, TCI), hydrazine monohydrate (N_2H_4, 64-65%, reagent grade, 98%, Sigma-Aldrich), potassium carbonate (K_2CO_3, 99.5%, Aldrich), potassium bicarbonate ($KHCO_3$, 99.7%, Aldrich), trioctylphosphine oxide (TOPO, 99%, Sigma-Aldrich), carbon black (CB, Vulcan XC72, Sigma Aldrich), and Nafion (10 wt.%, perfluorinated ion-exchange resin, dispersion in water, Sigma-Aldrich) were used as received without any further treatment. All chemical manipulation and ink preparation processes were carried out in an Ar-filled glovebox. Analytical grade chloroform and ethanol for the washing process were obtained from various sources. MilliQ water (18.2 MΩ cm) was used for electrolyte and ink preparation, and ion chromatography (IC) measurements. *Caution*: *1,2-ethanedithiol would release an unpleasant odour and should be carefully handled only in the fume hood and glovebox.*

NiS synthesis. Three steps were involved in the synthesis of NiS NPs (Scheme 1): i) Ink Preparation. To prepare a Ni−S molecular ink, elemental Ni (1 mmol) and S (1 mmol) powders were weighed and added to a glass vial (10 mL). En (3.3 mL) and Edt (0.3 mL) were sequentially added to the vial. The mixture was stirred at 750 rpm at room temperature for 24 hrs. These operations were conducted in the Ar-filled glovebox. ii) Solvent evaporation to obtain a dry powder. The obtained Ni-S molecular ink was filtered using a PTFE filter (0.45 μm) to remove the insoluble particles, and swiftly injected into a preheated (250 °C) three-neck flask. Ar was introduced into the flask from one neck, while the other neck was connected to the vacuum to quickly remove the vapour coming from the ink. A safety flask containing water/ethanol was placed between the vacuum and reaction flask to collect the vapour emanating from the ink solution. Upon ink injection, the temperature decreased and then increased slowly to 250 °C. The flask was then kept at this temperature to obtain a dry powder (generally within 10 min). The product was then grounded into fine powder for the

following annealing treatment. iii) Annealing of dry powder. The collected dry powder was placed in a tubular furnace under Ar atmosphere at 300 °C for 1 h, and then at 400 °C for additional 30 mins. A ramp rate of 3 °C/min was adopted. The annealed powder was collected and stored in the glovebox for further use.

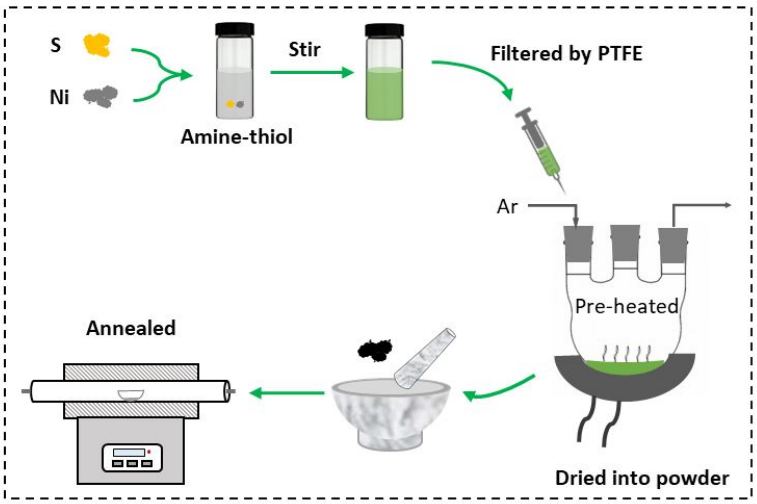

Scheme 1. Protocol for the synthesis of NiS NPs through an amine-thiol system.

Ni synthesis: Ni NPs were prepared following the procedure described in previous literature.[37] Typically, a three-neck flask was loaded with a magnetic bar, 1 mmol $Ni(acac)_2$, 7 ml OAm, 0.4 mmol TOP and 0.25 mmol TOPO, and the temperature was kept at 130 °C for 30 min with a gentle flow of argon. Then, the flask was quickly heated to 215 °C and maintained at this temperature for 45 min. Subsequently, the flask was cooled down to room temperature using a water bath. The black precipitate was separated through centrifugation after adding ethanol. To further remove the residual ligands on the surface before exploring the electrochemical performance, the precipitated NPs were dispersed in a mixture containing 28 mL acetonitrile and 0.8 mL hydrazine hydrate and stirred for at least 2 hours. The NPs were then collected by centrifugation and washed with acetonitrile 3 times. Finally, the Ni NPs were dried under vacuum.

Characterization: X-ray diffraction (XRD) was used to study the crystal structure on a Bruker AXS D8 Advance (Cu K radiation: λ = 1.5106 Å). Transition electron microscopy (TEM) images were obtained using ZEISS LIBRA 120, operating at 120 kV. High-resolution

TEM (HRTEM) together with scanning TEM (STEM) was investigated on a field emission gun FEI Tecnai F20 microscope. High angle annular dark-field (HAADF) STEM was combined with electron energy loss spectroscopy (EELS) in the Tecnai microscope by using a GATAN QUANTUM filter. The representative atomic model has been created with the Rhodius software.[38–40] X-ray photoelectron spectroscopy (XPS) analyses were conducted on a SPECS system.

Electrochemical measurements: Electrochemical performance was studied using a conventional three-electrode system, including a Hg/HgO reference electrode (RE), a Pt wire as the counter electrode (CE), and a 5 mm diameter glassy carbon (GC) as the working electrode (WE). To prepare the WE, firstly 5 mg of dried NPs and 10 mg of CB were dispersed in a vial containing 2 ml of MilliQ water/ethanol (v/v = 1:1) and 100 µL of a 10 wt% Nafion solution, followed by 1 h vigorous sonication. Afterwards, 5 µL of prepared ink were drop-casted on the top of a carefully polished GC electrode, and then allowed to dry naturally in the open air. Before the measurement, the alkaline electrolyte was bubbled with high-purity N_2 gas for half an hour. Conventional voltammetry techniques, including cyclic voltammetry (CV) and chronoamperometry (CA), were used to study the electrocatalytic property of the NPs. Electrochemical impedance spectra (EIS) were obtained in 1 M KOH with or without the presence of 1 M alcohols from 10^5 to 10^{-1} Hz. All obtained potentials (*vs.* Hg/HgO) were converted to the reversible hydrogen electrode (RHE) reference according to the Nernst equation: $E_{RHE} = E_{Hg/HgO} + 0.059x\text{pH} + E^{\Theta}_{Hg/HgO}$, where $E_{Hg/HgO}$ is the measured potential, $E^{\Theta}_{Hg/HgO}$ is the reference potential of 0.098 V, and pH is 13.6 as it corresponds to the actual value in 1 M KOH solution. To analyze the product of the oxidation reaction at the anode and calculate the faradaic efficiency, 0.5 mL of the solution was collected, diluted in 8 mL MilliQ water, and then analyzed by IC. A freshly prepared solution containing 4.5 mM KCO_3 and 0.8 mM $KHCO_3$ was used as leachate solution during the IC measurement. The amount of product was quantified with a standard curve based on the known ion concentrations. Then, the Faradaic efficiency (FE) was calculated using the equation: $FE(\%) = \frac{mol\ of\ product \times n \times F}{total\ charge\ passed} \times 100\%$, where n is the electron transfer number, F is the Faradaic constant (96485 C mol^{-1}), and the total charge passed is the electrons passed through the anode during the testing period.

Computational method: All the density functional theory (DFT) calculations were performed on the Vienna ab initio package (VASP) within the generalized gradient approximation (GGA) using the PBE formulation.[41–43] The projected augmented wave (PAW) potential was used to describe the ionic cores and valence electrons were taken into account using a plane-wave basis set with a kinetic energy cutoff of 400 eV.[44,45] Partial occupancies of the Kohn−Sham orbitals were allowed using the Gaussian smearing method and a width of 0.05 eV. The electronic energy was considered self-consistent when the energy change was smaller than 10^{-5} eV. Geometry optimization was considered convergent when the force change was smaller than 0.02 eV/Å. Grimme's DFT-D3 methodology was used to describe the dispersion interactions.[46]

Using a 7×11×9 Monkhorst-Pack k-point grid for Brillouin zone sampling, the equilibrium lattice constants of the monoclinic NiOOH unit cell were optimized to be a=5.168 Å, b=2.847 Å, c=4.516 Å, at α=90°, β=107.1°, γ=90°. They were used to construct a NiOOH(001) surface model with *p*(2×3) periodicity in the x and y directions and 1 stoichiometric layer in the z-direction separated by a vacuum layer in the depth of 15 Å to separate the surface slab from its periodic duplicates. One O atom was removed to create an oxygen vacancy. During structural optimizations, the gamma point in the Brillouin zone was used for k-point sampling, and all atoms were allowed to relax.

The free energy of a gas phase molecule or an adsorbate on the surface was calculated by the equation G = E + ZPE − TS, where E is the total energy, ZPE is the zero-point energy, T is the temperature in kelvin (298.15 K), and S is the entropy.

Results and Discussion

Nickel sulfide particles were produced from the decomposition of an alkahest-based ink prepared from elemental nickel and sulfur powders, followed by a post-annealing treatment (see experimental section and Scheme 1). Figure 1a shows the XRD pattern of the obtained material that can be indexed to a hexagonal NiS phase (JCPDS No. 01-075-0613). TEM characterization showed the obtained particles to have an average diameter of around 11 nm (Figure 1b). The STEM-EELS chemical composition maps shown in Figure 1c demonstrate a uniform distribution of both Ni and S. SEM-EDS analysis showed the Ni:S atomic ratio to be ca. 1:1 (Figure S1). HRTEM images (Figure 1d) showed the NiS NPs to have good crystallinity and confirmed the NiS hexagonal phase (space group =P63/mmc) with a=b=3.4480 Å, c=5.3850 Å. With the information obtained from the power spectrum analysis, the atomic model corresponding to the imaged NP has been created to visualize, from an atomistic point of view, the NP morphology and elemental distribution.

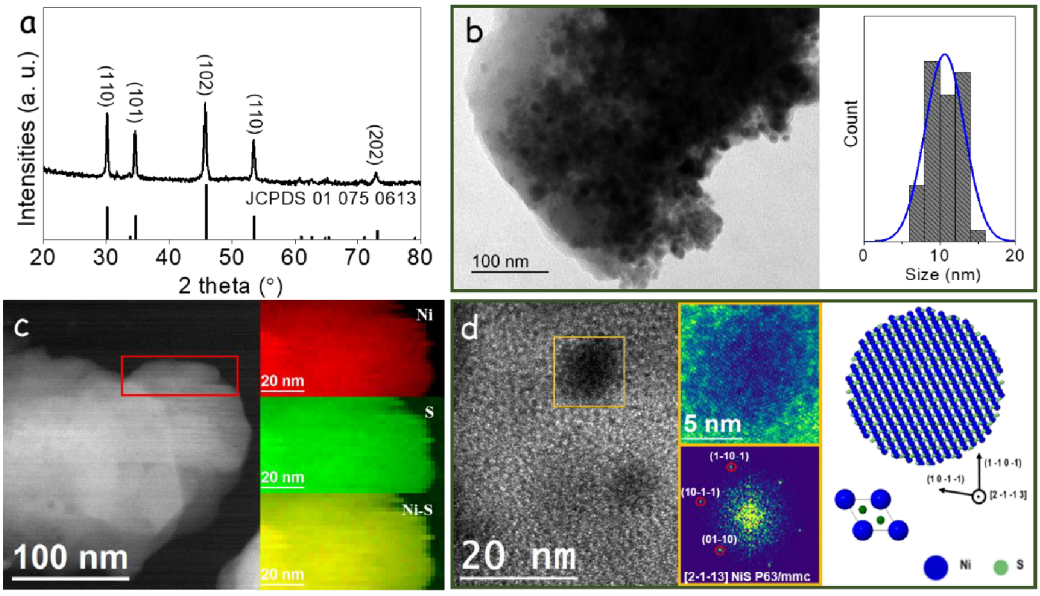

Figure 1. (a). XRD pattern of the as-synthesized NiS powder. (b) Representative TEM micrograph and the corresponding size distribution histogram of NiS NPs. (c) STEM-EELS chemical composition maps obtained from the red squared area of the STEM micrograph. Individual Ni $L_{2,3}$-edges at 855 eV (red), S $L_{2,3}$-edges at 165 eV (green) and composites of Ni-S. (d) HRTEM micrograph, detail of the orange squared region, and its corresponding power spectrum, The lattice fringe distances of this particle were measured to be 0.261 nm, 0.268 nm, and 0.298 nm, at 51.48º and 117.09º, which corresponds to the structure visualized

along its hexagonal [2-1-13] zone axis. The corresponding atomic supercell model of the NiS NP is also displayed and its 1*1*1 unit crystal model is also identified.

XPS spectra were collected to study the surface composition and atomic valence states (Figure S2). The Ni $2p_{3/2}$ XPS spectrum displayed three peaks, at 852.2 eV, 855.0 eV and 860.6 eV, which were associated with Ni within the NiS lattice, a Ni oxide or sulfoxide phase and a satellite peak, respectively.[47] The S 2p XPS spectrum displayed three doublets with the S 2p peak at 167.5 eV, 163.1 eV, and 160.9 eV that were assigned to sulfur oxides, NiS and surface sulfur or S-C, respectively.[48] These fitting characteristics of the XPS spectra are in good agreement with previous reports based on nickel and sulfur elements.[27,49–51]

To compare the electrocatalytic performance of NiS NPs with monometallic Ni, spherical Ni NPs with an average diameter of 11 nm were synthesized according to a previous report.[37] The XRD pattern and representative TEM images of the obtained particles can be found in Figure S3.

Working electrodes were prepared by drop-casting an ink containing a composite of Ni or NiS NPs and carbon black on a glassy carbon electrode. Using a conventional three-electrode system, the electrocatalytic activity of both electrodes was first studied in 1 M KOH solution via CV at a scan rate of 50 mV s^{-1} in the applied potential range of 0.9-1.7 V vs. RHE (black curves in Figure 2a for NiS, and Figure S4 for Ni).

In alkaline media, the surface of the Ni and NiS is hydroxidized into $Ni(OH)_2$ (equation 1).[52] Upon increasing the external potential, the $Ni(OH)_2$ oxidizes to NiOOH (equation 2). This oxidation took place at 1.32 V for both Ni- and NiS-based electrodes. Subsequently, a distinct peak was recorded at 1.34 V for the NiS (Figure 3a), and 1.43 V for the Ni electrode (Figure S4). When increasing the potential above ca. 1.65 V, oxygen started to evolve (equation 3).

$$Ni + 2OH^- \rightarrow Ni(OH)_2 + 2e^- \quad (1)$$

$$Ni(OH)_2 + OH^- \rightarrow NiOOH + H_2O + e^- \quad (2)$$

$$NiOOH + OH^- \rightarrow Ni(OH)_2 + O_2 + e^- \quad (3)$$

By adding 1 M methanol into the 1 M KOH electrolyte (olive curves), for NiS a sharp increase in the current density was obtained at ca. 1.342 V, just after NiOOH was formed. In

the presence of 1 M ethanol (blue curves), the current density started to increase at ca. 1.311 V in NiS, also along with the oxidation of $Ni(OH)_2$ to NiOOH. With the reference Ni electrode, the oxidation potential of ethanol was also lower than that of methanol for both electrodes (Figure S4).[53]

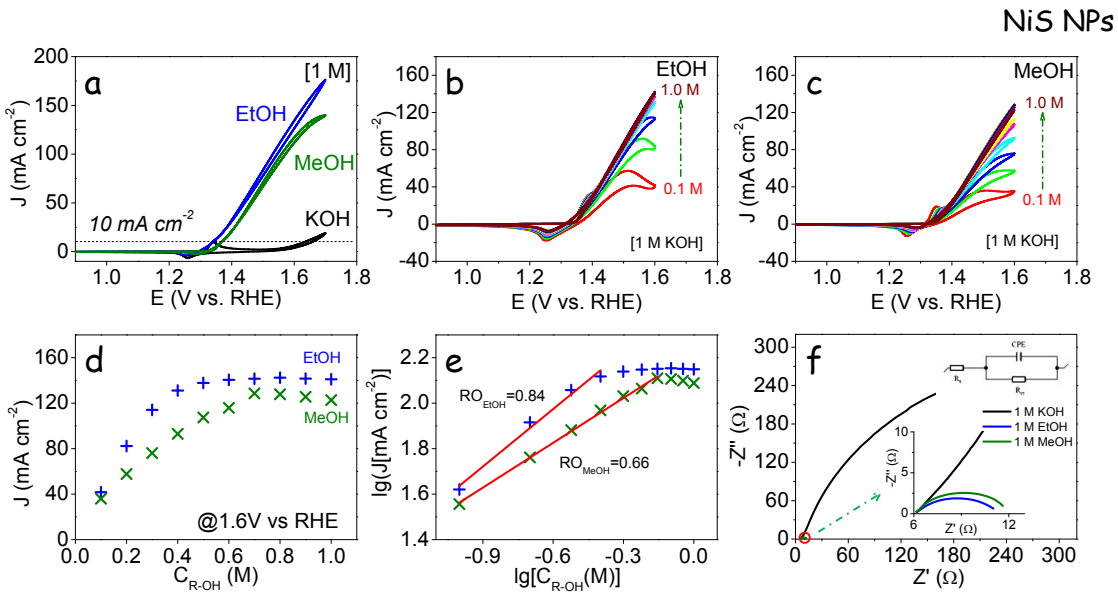

Figure 2. Electrochemical performance of a NiS-based electrode in 1 M KOH electrolyte. (a) CV curves without and with 1 M methanol or ethanol at a scan rate of 50 mV s^{-1}. (b-c) CV curves as a function of methanol and ethanol concentration from 0.1 M to 1 M. (d-e) Current density at 1.6 V vs RHE as a function of methanol and ethanol concentration, and the corresponding reaction order. (f) Nyquist plots of the impedance data obtained from a NiS electrode in 1 M KOH with and without 1 M methanol and ethanol at 1.5 V. Note that the current densities (J) were referred to the measured current (i) with the geometrical area of the GC electrode, i.e. 0.196 cm^{-2}.

For the NiS-based electrode, the potential required to generate a current density of 10 mA cm^{-2} in 1 M KOH was 1.635 V for OER. For MOR and EOR, the potentials required to generate a current density of 10 mA cm^{-2} in the presence of 1 M methanol and ethanol were 1.368 V and 1.339 V, respectively. As expected, the presence of alcohols in the alkaline media largely reduced the required potential, demonstrating the replacement of the sluggish OER at the cathode. In this context, much less energy was required to produce the same amount of hydrogen by coupling the EOR and MOR to the HER in alkaline media. These values were significantly lower than those obtained from the Ni-based electrode, 1.723 V in 1 M KOH, and 1.401 V and 1.360 V in the presence of 1 M methanol and ethanol, respectively.

Thus the use of NiS precursor NPs to produce the active NiOOH significantly improved the electrochemical activity.

Figures 2bc displays the CVs of 1 M KOH containing different concentrations of methanol and ethanol, from 0.1 M to 1 M. Both curves show a rapid increase of current density with the increase of the alcohol concentration. However, as observed in Figure 2d, where the current density at 1.6 V is plotted, a plateau is reached for concentrations around 0.5 and 0.6 M. The plateau is reached at smaller concentrations of ethanol than methanol, which is consistent with the higher activities obtained with ethanol, thus resulting in a saturation of the active sites at small concentrations. A linear dependence between the logarithmic current density and concentration at low concentrations was observed. From this linear region, a reaction order (RO) of 0.84 for ethanol and 0.66 for methanol were determined.[54] Similar values were obtained from the Ni electrode, 0.71 for ethanol and 0.64 for methanol (Figure S5), which were consistent with those obtained in previous reports.[11,55,56]

The Nyquist plots of the impedance response measured at 1.5 V versus RHE on the NiS-based electrode in 1 M KOH with and without ethanol or methanol are shown in Figure 2f. Compared with the semicircle radius in 1 M KOH, a smaller one for ethanol and methanol was exhibited. Impedance responses were fitted with an equivalent circuit (Figure 2f, inset). Fitting results revealed an enhanced charge-transfer process in ethanol and methanol with a R_{ct} of 4.2 Ω and 5.3 Ω (Table S1), two orders of magnitude lower than that obtained in 1 M KOH (462.9 Ω).

The electrochemical activity in the alkaline media, without the presence of alcohols, reveals the intrinsic properties of the catalyst itself. The measurement of CVs at different scan rates in the non-faradaic region allows for estimating the electrochemical surface area (ECSA).[57] As shown in Figure 3a, a double layer was observed in the 0.9-1.0 V potential window at the scan rate of 10-100 mV s^{-1}. Figure 3b presents a linear fitting between the current (i) at 0.95 V and scan rates with a slope of 3.1 and 2.1×10^4 at the forward and backward sweep, yielding its capacitance (C_{dl}). For both materials, ECSA was calculated by dividing C_{dl} by a specific capacitance (C_s) of 0.04 mF cm^{-2}, a typical number based on values reported for metal electrodes in an aqueous NaOH solution.[58] The ECSA value for NiS-based electrode was

found to be 6.4 cm^2, slightly above that of Ni NPs electrode (5.5 cm^2, Figure S6). It should be noted that the difference in the ECSA value between the NiS and Ni NPs could be slightly modified if considering different values for the specific capacitance.[57]

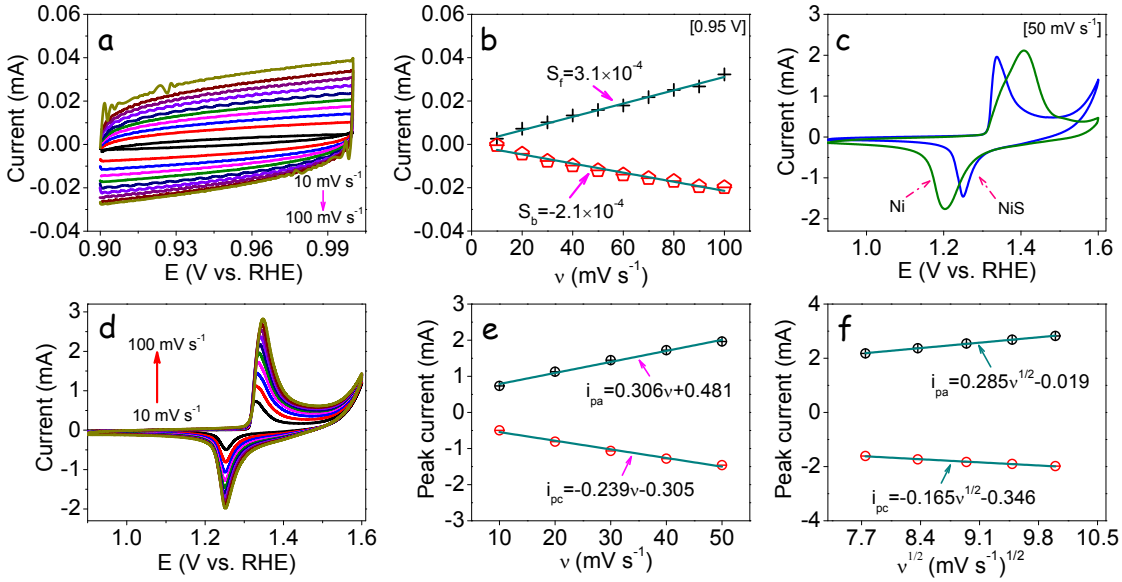

Figure 3. Electrochemical activity of a NiS-based electrode in 1 M KOH. (a) CV curves in the potential range of 0.9-1.0 V at different scan rates. (b) Current collected at 0.95 V in the forward and backward scan as a function of scan rates, and the corresponding linear fitting. (c) Comparison of the CV curve of NiS and Ni electrodes in the applied potential window of 0.9-1.6 V at the scan rate of 50 mV s^{-1}. (d) CV curves in the potential range of 0.9-1.6 V at different scan rates. (e) Linear fitting between the peak current and scan rates from 10 to 50 mV s^{-1}. (f) Linear fitting between the peak current and square root of scan rates from 60 to 100 mV s^{-1}.

Figure 3c compares the CV curve for NiS and Ni electrodes in 1 M KOH. As can be seen, the NiOOH on both electrodes starts to form at the same potential, ca. 1.309 V, but reached its maximum at clearly different potential values. A maximum current of 1.961 mA at 1.337 V was obtained for the NiS electrode, and 2.118 mA at 1.408 V for the Ni one. In the cathodic scan, the current peaks were located at 1.465 V and 1.204 V, with current values of -1.249 mA and -1.764 mA, for NiS and Ni electrodes, respectively. The potential difference of redox peaks (ΔE_p) for NiS electrode was determined to be 0.086 V, significantly below the 0.204 V obtained for the Ni electrode. These results indicate a much faster rate of electron transfer between the electrode surface and the active centers in NiS-based compared with Ni-based electrodes.[59]

The surface coverage of active species and the diffusion coefficient are important parameters that determine electrocatalytic performance. As shown in Figures 3d and S7a, a set of CVs was recorded at different scanning rates. As the scanning rate increases, larger oxidation/reduction peaks of $Ni(OH)_2 \Leftrightarrow NiOOH$ were measured.[54] Using the small scanning rate range, by plotting the peak current as a function of the scanning rate, the active surface coverage of NiOOH (Γ*) can be calculated (see the calculations in SI). For the NiS electrode, Γ* was determined to be 1.48×10^{-6} mol cm^{-2} (Figure 3e), an order magnitude above that of the Ni electrode (1.61×10^{-7} mol cm^{-2}, Figure S7b). In the high scanning rate range, the peak oxidation/reduction current densities can be linearly fitted with the square root of the scan rate. This linear dependence demonstrates the $Ni(OH)_2$/NiOOH redox reaction at NiS and Ni electrodes to be diffusion-limited (Figure 3f).[54] From the Randles equation, the diffusion coefficient was evaluated to be 3.78×10^{-7} cm^2 s^{-1} for NiS, slightly higher than that obtained for Ni, 3.13×10^{-7} cm^2 s^{-1} (Fig. S7c).

To evaluate the electrochemical stability of NiS and Ni catalysts, long-term CA tests were carried out in 1 M KOH solution with 1 M ethanol and methanol (Figures 4a and S8a). The current density for NiS was found to decrease relatively rapidly during the hour, to later approximately stabilize. The initial EOR and MOR current densities were 175.5 and 145.2 mA cm^{-2} on the NiS electrode. After a 10,000 s reaction, the current density was still 87.6 and 82.5 mA cm^{-2} for EOR and MOR. A similar decay trend was observed with the Ni electrode, maintaining 75.7 and 45.2 mA cm^{-2} for ethanol and methanol after the 10,000 s test, respectively (Figure S8a). Both the initial and the retained current density for the NiS-based electrode were higher than that of the reference Ni-based electrode and most previously reported catalysts (Table S2). In terms of stability, a severe decay in the activity was seen for both NiS- and Ni-based electrodes, which is also consistent with previous Ni-related studies (Table S2).

As shown in Figure S9, the XPS spectra of the NiS electrode after the long-term CA test demonstrates that a larger amount of sulfur oxides (SO_x) remain attached to the NiS surface (Figure S2). Besides, the high-resolution Ni 2p XPS spectrum shows the surface of the NiS to be completely oxidized to $Ni(OH)_2$ or NiOOH. DFT calculations show the optimized

NiOOH-SO_x structural model (Figure S10a). Compared with that of pristine NiOOH, the d electrons of Ni in the SOx-decorated NiOOH significantly concentrate around the Fermi level, thus improving the electroconductivity and electron transfer (Figure S10b). Thus, the higher performance of the NiS-based electrode may be in part associated with the presence of SO_x species during the electrocatalytic process, in agreement with previous publications.[29,60,61]

To calculate the Faradaic efficiency for the ethanol and methanol conversion process, the electrolyte obtained at the end of CA testing was analyzed by the means of IC. As shown in Figures 4b and S8b, a downward peak for water was presented at 2.8 min, and upward peaks at 4.3 min and 4.8 min, corresponding to the acetate and formate, were observed as the main products of the ethanol and methanol oxidation, respectively.[11] By comparing with a standard curve, 0.47 mmol acetate and 0.45 mmol formate were electrochemically produced for the NiS-based electrode. Thus, the FE was determined to be 98.0% for MOR and 80.9% for EOR. For monometallic Ni-based electrodes, over 10,000 s test in 1 M KOH with 1 M methanol, 0.27 mmol formate was produced with a FE of 96.6% (Figure 4c). For electrooxidation of ethanol, 0.32 mmol acetate was detected and the calculated FE was 76.7% (Figure 4c). Very close methanol-to-formate and ethanol-to-acetate FEs were obtained from both electrodes, thus the presence of S did not change the reaction selectivity.

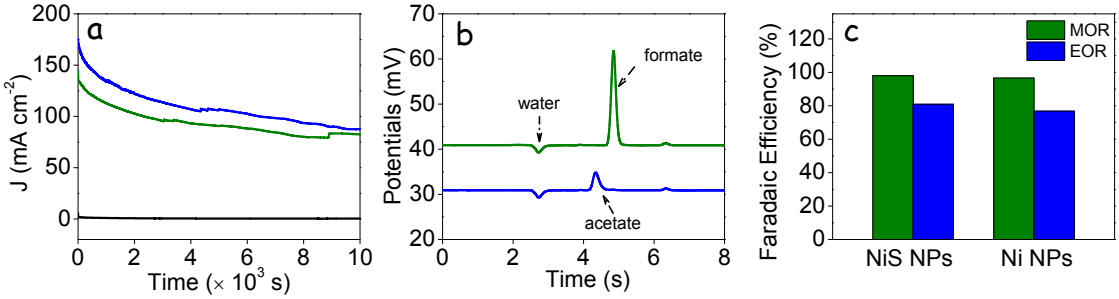

Figure 4. (a) CA test towards MOR (blue), EOR (green), and comparative curve (black, without alcohols) on NiS NPs electrode over 10,000 s testing period in 1 M KOH at 1.6 V.(b) IC curve of the solution at the end of CA testing. (c) Comparison of Faradaic efficiency between the NiS and Ni-electrodes.

Concerning that the current density of C2 ethanol oxidation is higher than that of C1 methanol oxidation both on the NiS and Ni electrode (Figures 2a and S4), it is interesting to compare

the dehydrogenation steps during the electrochemical process. Thus, we conducted DFT to understand and compare the EOR and MOR pathways. Considering that the NiOOH is the main active phase for the methanol and ethanol electrooxidation, we built a NiOOH(001) surface model to calculate the energy variation at steps of stable adsorption configurations of intermediates (as shown Figure 5a). According to previous reports, the alcohol oxidation process on the surface of Ni-based catalysts in alkaline media, which is accompanied by the reduction of NiOOH to $Ni(OH)_2$, takes place through the following steps:[21]

$$NiOOH + OH^- + HCH_2OH^* \rightarrow HCH_2O^* + Ni(OH)_2 + H_2O + e \quad (4)$$

$$NiOOH + OH^- + HCH_2O^* \rightarrow HCHO^* + Ni(OH)_2 + H_2O + e \quad (5)$$

$$NiOOH + OH^- + HCHO^* \rightarrow HCO^* + Ni(OH)_2 + H_2O + e \quad (6)$$

$$NiOOH + OH^- + HCO^* \rightarrow HCOOH^* + Ni(OH)_2 + H_2O + e \quad (7)$$

As shown in Figure 5b, the adsorption energy for methanol is larger than that of ethanol, (-0.25 eV for CH_3OH, and -0.14 eV for CH_3CH_2OH adsorption from the gas phase). As a second step, a reaction energy of 0.39 eV for the first dehydrogenation from CH_3OH to methoxy HCH_2O was calculated. This value is significantly lower than that of CH_3CH_2OH to ethoxy CH_3CH_2O, 0.82 eV. The second dehydrogenation step of R-CH_2O is exothermic by -0.45 eV for ethanol, CH_3CH_2O to CH_3CHO, while endothermic by 0.30 eV for methanol, HCH_2O to HCHO. The next step requires a reaction energy of 0.16 eV for the dehydrogenation of CH_3CHO to CH_3CO, well below that of the dehydrogenation of HCHO to HCO, 0.45 eV. Lastly, the adsorbed CH_3CO and HCO are endothermically released when interacting with OH^- ions in the alkaline media to form CH_3COOH and HCOOH, respectively. Overall, based on the calculated energy landscape illustrated in Figure5, the EOR requires overcoming total reaction energy of 0.82 eV, while MOR involves 3 consecutive endodermal dehydrogenation HCH_2OH to HCO with total reaction energy of 1.25 eV, which explains the higher current densities measured for EOR compared with MOR.

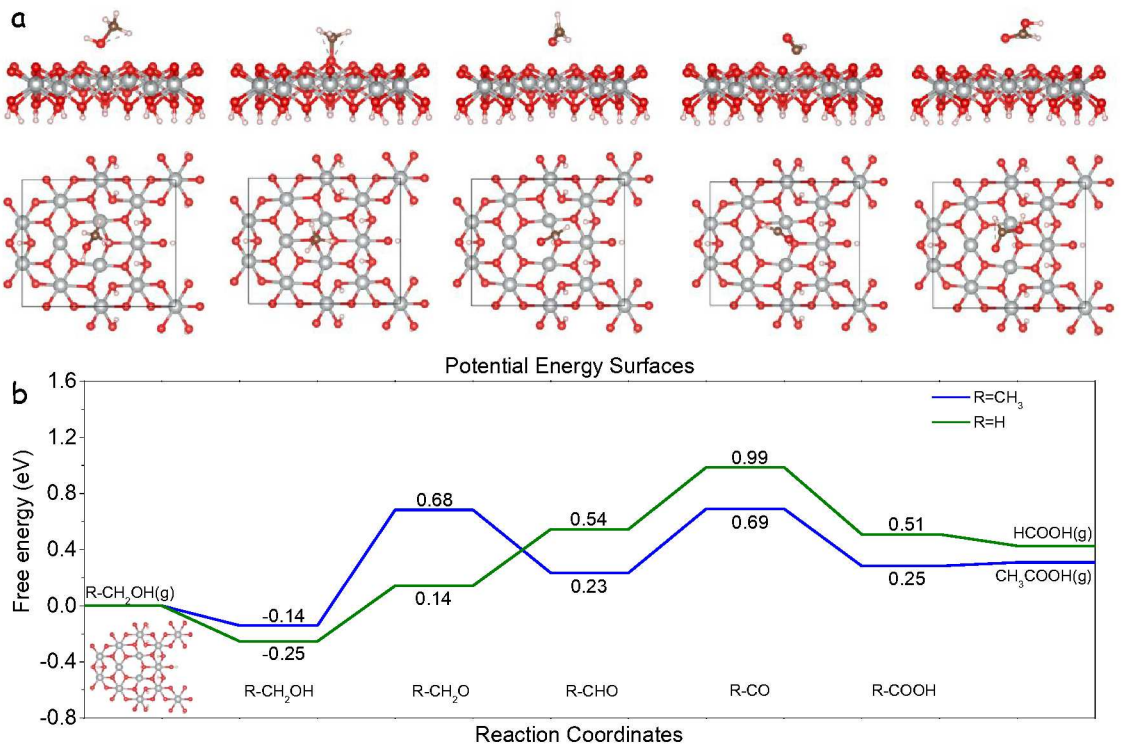

Figure 5. (a) Stable adsorption configurations of intermediates involved in the process of MOR on the NiOOH surface from the side and top view. (b) Computed methanol (red) and ethanol (black) electro-oxidation reaction pathways on NiOOH (110). The free energy of each configuration is displayed in black and given in eV.

Conclusion

In summary, we reported an ink precursor method to produce nickel sulfide NPs. The electrocatalytic performance toward MOR and EOR in alkaline media was thoroughly tested. Experimental investigations reveal the produced NiS to display excellent electrocatalytic performance associated with a higher ECSA and the presence of sulfate ions on the formed NiOOH surface in basic media. FEs well above 95% and 80% were obtained for MOR to formate and EOR to acetate, respectively. The presence of S resulted in a notable increase of activity, with 0.45 mmol acetate and 0.47 mmol formate on NiS-based electrode over 10000s CA testing, almost twofold above the obtained on Ni NPs-based electrode. Density functional theory calculations demonstrate the presence of the generated sulfate groups to modify the electronic properties of the NiOOH surface, improving electroconductivity and electron

transfer. Besides, DFT calculations demonstrate a more favourable reaction pathway for the decomposition of ethanol with a total required reaction energy of 0.82 eV, leading to higher performance than that of methanol decomposition involving 3 consecutive endodermal dehydrogenation HCH_2OH to HCO with total reaction energy of 1.25 eV. Overall, this study provides a better understanding of the electrocatalytic alcohol oxidation mechanism and paves the way for further advancing the catalyst in related fields.

Author Information

Corresponding Author

*Dr. Luming Li: liluming@cdu.edu.cn

*Dr. Yong Zuo: yongzuo16@gmail.com

*Prof. Andreu Cabot: acabot@irec.cat

Supporting Information

The Supporting Information is available free of charge at *XXXXXX*.

Structure and surface characterization including SEM, EDS, XPS, XRD, and TEM for Ni and/or NiS NPs, additional electrochemical measurements, fitting parameters for the Nyquist curve for NiS NPs, comparison of electrocatalytic performance, IC curve for Ni NPs, and DFT calculation including optimized structural model and the DOS (PDF).

Acknowledgements

This work was supported by the start-up funding at Chengdu University and also from the Natural Science Foundation of Sichuan (NSFSC) project funded by the Science and Technology Department of Sichuan Province (2022NSFSC1229). It was also supported by the European Regional Development Funds and by the Spanish Ministerio de Ciencia e Innovación through the project COMBENERGY (PID2019-105490RB-C32). T. Zhang is grateful to the China Scholarship Council (CSC) for scholarship support. T. Zhang, M.C. Spadaro and J. Arbiol acknowledge funding from Generalitat de Catalunya 2017 SGR 327. ICN2 acknowledges support from the Severo Ochoa Programme (MINECO, Grant no.

SEV-2013-0295). T. Zhang has received funding from the CSC-UAB PhD scholarship program. M. C. Spadaro has received funding from the postdoctoral fellowship Juan de la Cierva from MICINN (IJCI-2019) and the Severo Ochoa programme. ICN2 authors thank support from the project NANOGEN (PID2020-116093RB-C43), funded by MCIN/ AEI/10.13039/501100011033/. IREC and ICN2 are funded by the CERCA Programme / Generalitat de Catalunya. Part of the present work has been performed in the framework of Universitat Autònoma de Barcelona Materials Science PhD program.

Conflict of interest

The authors declare no competing financial interest.

Reference

(1) Chu, S.; Majumdar, A. Opportunities and Challenges for a Sustainable Energy Future. *Nature* **2012**, *488* (7411), 294–303.

(2) Sartbaeva, A.; Kuznetsov, V. L.; Wells, S. A.; Edwards, P. P. Hydrogen Nexus in a Sustainable Energy Future. *Energy Environ. Sci.* **2008**, *1* (1), 79–85.

(3) You, B.; Sun, Y. Innovative Strategies for Electrocatalytic Water Splitting. *Acc. Chem. Res.* **2018**, *51* (7), 1571–1580.

(4) Wu, S.; Zhu, Y.; Yang, G.; Zhou, H.; Li, R.; Chen, S.; Li, H.; Li, L.; Fontaine, O.; Deng, J. Take Full Advantage of Hazardous Electrochemical Chlorine Erosion to Ultrafast Produce Superior NiFe Oxygen Evolution Reaction Electrode. *Chem. Eng. J.* **2022**, *446*, 136833.

(5) Xiang, K.; Wu, D.; Deng, X.; Li, M.; Chen, S.; Hao, P.; Guo, X.; Luo, J. L.; Fu, X. Z. Boosting H_2 Generation Coupled with Selective Oxidation of Methanol into Value-Added Chemical over Cobalt Hydroxide@Hydroxysulfide Nanosheets Electrocatalysts. *Adv. Funct. Mater.* **2020**, *30* (10), 1909610.

(6) Luo, H.; Barrio, J.; Sunny, N.; Li, A.; Steier, L.; Shah, N.; Stephens, I. E. L.; Titirici, M. M. Progress and Perspectives in Photo- and Electrochemical-Oxidation of Biomass for Sustainable Chemicals and Hydrogen Production. *Adv. Energy Mater.* **2021**, 2101180.

(7) Wu, D.; Hao, J.; Song, Z.; Fu, X. Z.; Luo, J. L. All Roads Lead to Rome: An Energy-Saving Integrated Electrocatalytic CO_2 Reduction System for Concurrent Value-Added Formate Production. *Chem. Eng. J.* **2020**, 127893.

(8) Wang, Q.; Liu, J.; Li, T.; Zhang, T.; Arbiol, J.; Yan, S.; Wang, Y.; Li, H.; Cabot, A. Pd2Ga Nanorods as Highly Active Bifunctional Catalysts for Electrosynthesis of Acetic Acid Coupled with Hydrogen Production. *Chem. Eng. J.* **2022**, *446*, 136878.

(9) Liu, Q.; Wu, L.; Gülak, S.; Rockstroh, N.; Jackstell, R.; Beller, M. Towards a Sustainable Synthesis of Formate Salts: Combined Catalytic Methanol Dehydrogenation and Bicarbonate Hydrogenation. *Angew. Chemie - Int. Ed.* **2014**, *53*

(27), 7085–7088.

(10) Li, J.; Wei, R.; Wang, X.; Zuo, Y.; Han, X.; Arbiol, J.; Llorca, J.; Yang, Y.; Cabot, A.; Cui, C. Selective Methanol-to-Formate Electrocatalytic Conversion on Branched Nickel Carbide. *Angew. Chemie - Int. Ed.* **2020**, *59* (47), 20826–20830.

(11) Li, J.; Xing, C.; Zhang, Y.; Zhang, T.; Spadaro, M. C.; Wu, Q.; Yi, Y.; He, S.; Llorca, J.; Arbiol, J.; Cabot, A.; Cui, C. Nickel Iron Diselenide for Highly Efficient and Selective Electrocatalytic Conversion of Methanol to Formate. *Small* **2021**, *17* (6), 2006623.

(12) You, B.; Liu, X.; Jiang, N.; Sun, Y. A General Strategy for Decoupled Hydrogen Production from Water Splitting by Integrating Oxidative Biomass Valorization. *J. Am. Chem. Soc.* **2016**, *138* (41), 13639–13646.

(13) Liu, Y. P.; Zhao, S. F.; Guo, S. X.; Bond, A. M.; Zhang, J.; Zhu, G.; Hill, C. L.; Geletii, Y. V. Electrooxidation of Ethanol and Methanol Using the Molecular Catalyst $[\{Ru_4O_4(OH)_2(H_2O)_4\}(\gamma\text{-}SiW_{10}O_{36})_2]_{10-}$. *J. Am. Chem. Soc.* **2016**, *138* (8), 2617–2628.

(14) Liu, C.; Zhou, W.; Zhang, J.; Chen, Z.; Liu, S.; Zhang, Y.; Yang, J.; Xu, L.; Hu, W.; Chen, Y.; Deng, Y. Air-Assisted Transient Synthesis of Metastable Nickel Oxide Boosting Alkaline Fuel Oxidation Reaction. *Adv. Energy Mater.* **2020**, 2001397.

(15) Han, C.; Li, W.; Shu, C.; Guo, H.; Liu, H.; Dou, S.; Wang, J. Catalytic Activity Boosting of Nickel Sulfide toward Oxygen Evolution Reaction via Confined Overdoping Engineering. *ACS Appl. Energy Mater.* **2019**, *2* (8), 5363–5372.

(16) Lee, M.; Oh, H. S.; Cho, M. K.; Ahn, J. P.; Hwang, Y. J.; Min, B. K. Activation of a Ni Electrocatalyst through Spontaneous Transformation of Nickel Sulfide to Nickel Hydroxide in an Oxygen Evolution Reaction. *Appl. Catal. B Environ.* **2018**, *233*, 130–135.

(17) Mabayoje, O.; Shoola, A.; Wygant, B. R.; Mullins, C. B. The Role of Anions in Metal Chalcogenide Oxygen Evolution Catalysis: Electrodeposited Thin Films of Nickel Sulfide as "Pre-Catalysts." *ACS Energy Lett.* **2016**, *1* (1), 195–201.

(18) Han, M. H.; Pin, M. W.; Koh, J. H.; Park, J. H.; Kim, J.; Min, B. K.; Lee, W. H.; Oh, H. S. Improving the Oxygen Evolution Reaction Using Electronic Structure Modulation of Sulfur-Retaining Nickel-Based Electrocatalysts. *J. Mater. Chem. A* **2021**, *9* (47), 27034–27040.

(19) Zhang, J.; Xu, C.; Zhang, D.; Zhao, J.; Zheng, S.; Su, H.; Wei, F.; Yuan, B.; Fernandez, C. Facile Synthesis of a Nickel Sulfide (NiS) Hierarchical Flower for the Electrochemical Oxidation of H_2O_2 and the Methanol Oxidation Reaction (MOR). *J. Electrochem. Soc.* **2017**, *164* (4), B92–B96.

(20) Jia, J.; Zhao, L.; Chang, Y.; Jia, M.; Wen, Z. Understanding the Growth of NiSe Nanoparticles on Reduced Graphene Oxide as Efficient Electrocatalysts for Methanol Oxidation Reaction. *Ceram. Int.* **2020**, *46* (8), 10023–10028.

(21) Zhao, B.; Liu, J.; Wang, X.; Xu, C.; Sui, P.; Feng, R.; Wang, L.; Zhang, J.; Luo, J. L.; Fu, X. Z. CO_2-Emission-Free Electrocatalytic CH_3OH Selective Upgrading with High Productivity at Large Current Densities for Energy Saved Hydrogen Co-Generation. *Nano Energy* **2021**, *80*, 105530.

(22) Ding, Y.; Xue, Q.; Hong, Q. L.; Li, F. M.; Jiang, Y. C.; Li, S. N.; Chen, Y. Hydrogen and Potassium Acetate Co-Production from Electrochemical Reforming of Ethanol at

Ultrathin Cobalt Sulfide Nanosheets on Nickel Foam. *ACS Appl. Mater. Interfaces* **2021**, *13* (3), 4026–4033.

(23) Zhang, Y.; Zhang, L.; Song, C.; Qin, Y.; Lu, L.; Zhu, W.; Zhuang, Z. Nickel Chalcogenides as Selective Ethanol Oxidation Electro-Catalysts and Their Structure-Performance Relationships. *Chem. Commun.* **2022**, *58* (15), 2496–2499.

(24) Yao Li; Shi, W.; Qu, Y.; Dai, T.; Li, J.; Zhao, Y.; Yu, J. NiS_2 Nanoparticles with Tunable Surface Area As Catalyst for Ethanol Oxidation. *Russ. J. Phys. Chem. A* **2019**, *93* (8), 1577–1583.

(25) Li, J.; Wang, X.; Xing, C.; Li, L.; Mu, S.; Han, X.; He, R.; Liang, Z.; Martinez, P.; Yi, Y.; Wu, Q.; Pan, H.; Arbiol, J.; Cui, C.; Zhang, Y.; Cabot, A. Electrochemical Reforming of Ethanol with Acetate Co-Production on Nickel Cobalt Selenide Nanoparticles. *Chem. Eng. J.* **2022**, 135817.

(26) Wu, T. H.; Lin, Y. C.; Hou, B. W.; Liang, W. Y. Nanostructured B−NiS Catalyst for Enhanced and Stable Electro−oxidation of Urea. *Catalysts* **2020**, *10* (11), 1–11.

(27) Kim, S. Y.; Gopi, C. V. V. M.; Reddy, A. E.; Kim, H. J. Facile Synthesis of a NiO/NiS Hybrid and Its Use as an Efficient Electrode Material for Supercapacitor Applications. *New J. Chem.* **2018**, *42* (7), 5309–5313.

(28) Li, J.; Smith, R. L.; Xu, S.; Li, D.; Yang, J.; Zhang, K.; Shen, F. Manganese Oxide as an Alternative to Vanadium-Based Catalysts for Effective Conversion of Glucose to Formic Acid in Water. *Green Chem.* **2022**, *24* (1), 315–324.

(29) Li, S.; Ma, R.; Hu, J.; Li, Z.; Liu, L.; Wang, X.; Lu, Y.; Sterbinsky, G. E.; Liu, S.; Zheng, L.; Liu, J.; Liu, D.; Wang, J. Coordination Environment Tuning of Nickel Sites by Oxyanions to Optimize Methanol Electro-Oxidation Activity. *Nat. Commun.* **2022**, *13* (1), 1–11.

(30) Webber, D. H.; Brutchey, R. L. Alkahest for V2VI3 Chalcogenides: Dissolution of Nine Bulk Semiconductors in a Diamine-Dithiol Solvent Mixture. *J. Am. Chem. Soc.* **2013**, *135* (42), 15722–15725.

(31) Lin, Z.; He, Q.; Yin, A.; Xu, Y.; Wang, C.; Ding, M.; Cheng, H. C.; Papandrea, B.; Huang, Y.; Duan, X. Cosolvent Approach for Solution-Processable Electronic Thin Films. *ACS Nano* **2015**, *9* (4), 4398–4405.

(32) McCarthy, C. L.; Brutchey, R. L. Solution Processing of Chalcogenide Materials Using Thiol-Amine "Alkahest" Solvent Systems. *Chem. Commun.* **2017**, *53* (36), 4888–4902.

(33) Zuo, Y.; Li, J.; Yu, X.; Du, R.; Zhang, T.; Wang, X.; Arbiol, J.; Llorca, J.; Cabot, A. A SnS2 Molecular Precursor for Conformal Nanostructured Coatings. *Chem. Mater.* **2020**, *32* (5), 2097–2106.

(34) Yu, X.; Luo, Z.; Zhang, T.; Tang, P.; Li, J.; Wang, X.; Llorca, J.; Arbiol, J.; Liu, J.; Cabot, A. Stability of Pd_3Pb Nanocubes during Electrocatalytic Ethanol Oxidation. *Chem. Mater.* **2020**, *32* (5), 2044–2052.

(35) Abdelkareem, M. A.; Sayed, E. T.; Mohamed, H. O.; Obaid, M.; Rezk, H.; Chae, K. J. Nonprecious Anodic Catalysts for Low-Molecular-Hydrocarbon Fuel Cells: Theoretical Consideration and Current Progress. *Progress in Energy and Combustion Science*. Elsevier Ltd March 1, 2020, p 100805.

(36) Bott-Neto, J. L.; Martins, T. S.; Machado, S. A. S.; Ticianelli, E. A. Electrocatalytic Oxidation of Methanol, Ethanol, and Glycerol on $Ni(OH)_2$ Nanoparticles Encapsulated

with Poly[Ni(Salen)] Film. *ACS Appl. Mater. Interfaces* **2019**, *11* (34), 30810–30818.

(37) Chen, Y.; Luo, X.; She, H.; Yue, G.-H.; Peng, D.-L. Size- and Structure-Controlled Synthesis and Characterization of Nickel Nanoparticles. *J. Nanosci. Nanotechnol.* **2009**, *9* (9), 5157–5163.

(38) Zhang, Y.; Xing, C.; Liu, Y.; Spadaro, M. C.; Wang, X.; Li, M.; Xiao, K.; Zhang, T.; Guardia, P.; Lim, K. H.; Moghaddam, A. O.; Llorca, J.; Arbiol, J.; Ibáñez, M.; Cabot, A. Doping-Mediated Stabilization of Copper Vacancies to Promote Thermoelectric Properties of $Cu_{2-x}S$. *Nano Energy* **2021**, *85*, 105991.

(39) Bernal, S.; Botana, F. J.; Calvino, J. J.; López-Cartes, C.; Pérez-Omil, J. A.; Rodríguez-Izquierdo, J. M. The Interpretation of HREM Images of Supported Metal Catalysts Using Image Simulation: Profile View Images. *Ultramicroscopy* **1998**, *72* (3–4), 135–164.

(40) Arbiol, J.; Cirera, A.; Peiró, F.; Cornet, A.; Morante, J. R.; Delgado, J. J.; Calvino, J. J. Optimization of Tin Dioxide Nanosticks Faceting for the Improvement of Palladium Nanocluster Epitaxy. *Appl. Phys. Lett.* **2002**, *80* (2), 329–331.

(41) Kresse, G.; Furthmüller, J. Efficiency of Ab-Initio Total Energy Calculations for Metals and Semiconductors Using a Plane-Wave Basis Set. *Comput. Mater. Sci.* **1996**, *6* (1), 15–50.

(42) Kresse, G.; Furthmüller, J. Efficient Iterative Schemes for Ab Initio Total-Energy Calculations Using a Plane-Wave Basis Set. *Phys. Rev. B - Condens. Matter Mater. Phys.* **1996**, *54* (16), 11169–11186.

(43) Perdew, J. P.; Burke, K.; Ernzerhof, M. Generalized Gradient Approximation Made Simple. *Phys. Rev. Lett.* **1996**, *77* (18), 3865–3868.

(44) Joubert, D. From Ultrasoft Pseudopotentials to the Projector Augmented-Wave Method. *Phys. Rev. B - Condens. Matter Mater. Phys.* **1999**, *59* (3), 1758–1775.

(45) Blöchl, P. E. Projector Augmented-Wave Method. *Phys. Rev. B* **1994**, *50* (24), 17953–17979.

(46) Grimme, S.; Antony, J.; Ehrlich, S.; Krieg, H. A Consistent and Accurate Ab Initio Parametrization of Density Functional Dispersion Correction (DFT-D) for the 94 Elements H-Pu. *J. Chem. Phys.* **2010**, *132* (15), 154104.

(47) Moulder, J. F.; Stickle, W. F.; Sobol, P. E.; Bomben, K. D. *Handbook of X-Ray Photoelectron Spectroscopy: A Reference Book of Standard Spectra for Identification and Interpretation of XPS Data*; 1992, 85, 86.

(48) Moulder, J. F.; Stickle, W. F.; Sobol, P. E.; Bomben, K. D. *Handbook of X-Ray Photoelectron Spectroscopy: A Reference Book of Standard Spectra for Identification and Interpretation of XPS Data*; 1992, 60, 61.

(49) Gopi, C. V. V. M.; Venkata-Haritha, M.; Ravi, S.; Thulasi-Varma, C. V.; Kim, S. K.; Kim, H. J. Solution Processed Low-Cost and Highly Electrocatalytic Composite NiS/PbS Nanostructures as a Novel Counter-Electrode Material for High-Performance Quantum Dot-Sensitized Solar Cells with Improved Stability. *J. Mater. Chem. C* **2015**, *3* (48), 12514–12528.

(50) Zuo, Y.; Liu, Y.; Li, J.; Du, R.; Yu, X.; Xing, C.; Zhang, T.; Yao, L.; Arbiol, J.; Llorca, J.; Sivula, K.; Guijarro, N.; Cabot, A. Solution-Processed Ultrathin SnS_2-Pt Nanoplates for Photoelectrochemical Water Oxidation. *ACS Appl. Mater. Interfaces* **2019**, *11* (7),

6918–6926.

(51) Li, J.; Zuo, Y.; Liu, J.; Wang, X.; Yu, X.; Du, R.; Zhang, T.; Infante-Carrió, M. F.; Tang, P.; Arbiol, J.; Llorca, J.; Luo, Z.; Cabot, A. Superior Methanol Electrooxidation Performance of (110)-Faceted Nickel Polyhedral Nanocrystals. *J. Mater. Chem. A* **2019**, *7* (38), 22036–22043.

(52) Cui, X.; Guo, W.; Zhou, M.; Yang, Y.; Li, Y.; Xiao, P.; Zhang, Y.; Zhang, X. Promoting Effect of Co in Ni_mCo_n (m+n=4) Bimetallic Electrocatalysts for Methanol Oxidation Reaction. *ACS Appl. Mater. Interfaces* **2015**, *7* (1), 493–503.

(53) Wang, H. Y.; Hsu, Y. Y.; Chen, R.; Chan, T. S.; Chen, H. M.; Liu, B. Ni^{3+}-Induced Formation of Active NiOOH on the Spinel Ni-Co Oxide Surface for Efficient Oxygen Evolution Reaction. *Adv. Energy Mater.* **2015**, *5* (10), 1500091.

(54) Cui, X.; Xiao, P.; Wang, J.; Zhou, M.; Guo, W.; Yang, Y.; He, Y.; Wang, Z.; Yang, Y.; Zhang, Y.; Lin, Z. Highly Branched Metal Alloy Networks with Superior Activities for the Methanol Oxidation Reaction. *Angew. Chemie - Int. Ed.* **2017**, *56* (16), 4488–4493.

(55) Li, J.; Luo, Z.; Zuo, Y.; Liu, J.; Zhang, T.; Tang, P.; Arbiol, J.; Llorca, J.; Cabot, A. NiSn Bimetallic Nanoparticles as Stable Electrocatalysts for Methanol Oxidation Reaction. *Appl. Catal. B Environ.* **2018**, *234*, 10–18.

(56) Wu, D.; Zhang, W.; Cheng, D. Facile Synthesis of Cu/NiCu Electrocatalysts Integrating Alloy, Core-Shell, and One-Dimensional Structures for Efficient Methanol Oxidation Reaction. *ACS Appl. Mater. Interfaces* **2017**, *9* (23), 19843–19851.

(57) Wei, C.; Sun, S.; Mandler, D.; Wang, X.; Qiao, S. Z.; Xu, Z. J. Approaches for Measuring the Surface Areas of Metal Oxide Electrocatalysts for Determining Their Intrinsic Electrocatalytic Activity. *Chem. Soc. Rev.* **2019**, *48* (9), 2518–2534.

(58) McCrory, C. C. L.; Jung, S.; Peters, J. C.; Jaramillo, T. F. Benchmarking Heterogeneous Electrocatalysts for the Oxygen Evolution Reaction. *J. Am. Chem. Soc.* **2013**, *135* (45), 16977–16987.

(59) Chen, D.; Minteer, S. D. Mechanistic Study of Nickel Based Catalysts for Oxygen Evolution and Methanol Oxidation in Alkaline Medium. *J. Power Sources* **2015**, *284*, 27–37.

(60) Zhao, B.; Xu, C.; Shakouri, M.; Feng, R.; Zhang, Y.; Liu, J.; Wang, L.; Zhang, J.; Luo, J. L.; Fu, X. Z. Anode-Cathode Interchangeable Strategy for in Situ Reviving Electrocatalysts' Critical Active Sites for Highly Stable Methanol Upgrading and Hydrogen Evolution Reactions. *Appl. Catal. B Environ.* **2022**, *305*, 121082.

(61) Zhao, B.; Liu, J.; Xu, C.; Feng, R.; Sui, P.; Wang, L.; Zhang, J.; Luo, J. L.; Fu, X. Z. Hollow NiSe Nanocrystals Heterogenized with Carbon Nanotubes for Efficient Electrocatalytic Methanol Upgrading to Boost Hydrogen Co-Production. *Adv. Funct. Mater.* **2021**, *31* (8), 2008812.

TOC

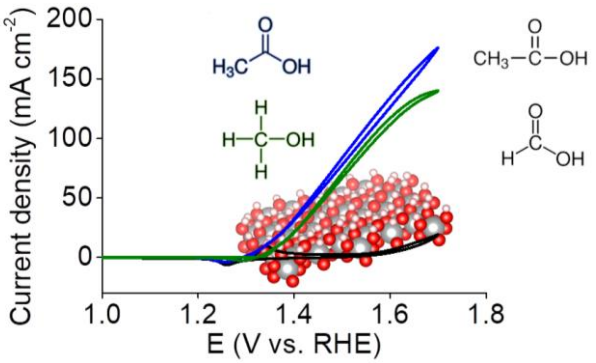

Nickel sulfide nanoparticles deliver excellent electrocatalytic activities toward alcohol oxidation, twofold above those of monometallic Ni particles, with 95% methanol-to-formate and 80% ethanol-to-acetate faradaic efficiencies. DFT calculations show a lower overall reaction energy for the dehydrogenation of ethanol than methanol, through a sequential three-step process, explaining the higher ethanol-to-acetate activity obtained.